AGU PUBLICATIONS

Geophysical Research Letters

RESEARCH LETTER
10.1002/2016GL069096

Key Points:
- Multispacecraft observations of a reflected EMIC-triggered emission
- The reflection makes the rising tone slope shallower
- High abundance of O^+ ions is required to match the group velocity observations

Correspondence to:
B. Grison,
grison@ufa.cas.cz

Citation:
Grison, B., F. Darrouzet, O. Santolík, N. Cornilleau-Wehrlin, and A. Masson (2016), Cluster observations of reflected EMIC-triggered emission, *Geophys. Res. Lett.*, *43*, 4164–4171, doi:10.1002/2016GL069096.

Received 12 APR 2016
Accepted 26 APR 2016
Accepted article online 2 MAY 2016
Published online 14 MAY 2016

Cluster observations of reflected EMIC-triggered emission

B. Grison[1], F. Darrouzet[2], O. Santolík[1,3], N. Cornilleau-Wehrlin[4], and A. Masson[5]

[1]Department of Space Physics, Institute of Atmospheric Physics, CAS, Prague, Czech Republic, [2]Royal Belgian Institute for Space Aeronomy (BIRA-IASB), Brussels, Belgium, [3]Faculty of Mathematics and Physics, Charles University, Prague, Czech Republic, [4]Laboratoire de Physique des Plasmas, CNRS/Ecole Polytechnique/Obs. de Paris/UPMC/Univ. Paris-Sud, Palaiseau, France, [5]Science Operations Department, ESAC, European Space Agency, Madrid, Spain

Abstract On 19 March 2001, the Cluster fleet recorded an electromagnetic rising tone on the nightside of the plasmasphere. The emission was found to propagate toward the Earth and toward the magnetic equator at a group velocity of about 200 km/s. The Poynting vector is mainly oblique to the background magnetic field and directed toward the Earth. The propagation angle $\theta_{\mathbf{k},\mathbf{B}_0}$ becomes more oblique with increasing magnetic latitude. Inside each rising tone $\theta_{\mathbf{k},\mathbf{B}_0}$ is more field aligned for higher frequencies. Comparing our results to previous ray tracing analysis we conclude that this emission is a triggered electromagnetic ion cyclotron (EMIC) wave generated at the nightside plasmapause. We detect the wave just after its reflection in the plasmasphere. The reflection makes the tone slope shallower. This process can contribute to the formation of pearl pulsations.

1. Introduction

Electromagnetic ion cyclotron (EMIC)-triggered emissions (TEs) have been observed in situ by the Cluster spacecraft at the nightside plasmapause [*Pickett et al.*, 2010]. Simulations and theory of the wave generation between the local Helium (He^+) and proton (H^+) gyrofrequencies (f_{He^+} and f_{H^+}, respectively) agree with the observations [*Omura et al.*, 2010; *Shoji and Omura*, 2011]. Simulations predict also TEs generation below f_{He^+} [*Shoji et al.*, 2011]. The triggering process of left-handed EMIC waves takes place close to the magnetic equatorial region in the presence of a hot proton population. TEs are observed at various locations close to the magnetic equatorial plane [*Nakamura et al.*, 2014; *He et al.*, 2014].

Grison et al. [2013] (we refer hereafter to this paper as paper 1) studied 8 years of Cluster data. The nightside plasmapause is the only part of the Cluster orbit where TEs with a large-frequency extent have been observed during a visual inspection of magnetic spectrograms. From the four reported cases in paper 1, the picture is clear in terms of polarization. The full circular left-hand polarization observed at magnetic latitudes (MLATs) lower than 5° quickly turns linear and even right hand above ~10° MLAT. The polarization reversal of EMIC waves at this latitude is explained by the presence of minor ion species [*Young et al.*, 1981]. For three of the Cluster cases, the emissions propagate clearly away from the equatorial region. The fourth case (19 March 2001 event) is the most puzzling: the rising tone frequency extends below the local f_{He^+}. The polarization is right handed, the tone slope is shallow, and the parallel component of the Poynting vector is difficult to interpret.

In what follows, we focus on this event, when a similar tone is observed by the four spacecraft. In section 2, we first detail the fleet instrumentation and location. Then we determine the propagation direction (section 3) and the group velocity of the rising tone (section 4). In section 5, our results are compared to the cold plasma theory and we discuss the wave journey with respect to previous ray tracing studies in section 6. Conclusions are given in section 7.

2. Observations

In 2001, the four Cluster satellites (C1, C2, C3, and C4) fly in a tetrahedral configuration along similar elliptical polar orbits with a perigee of about 4 Earth radii (R_E) [*Escoubet et al.*, 1997]. They traverse the inner magnetosphere, and usually the plasmasphere, from the Southern Hemisphere to the Northern Hemisphere every 57 h. Each Cluster satellite contains 11 identical instruments, including the Electric Field and Wave (EFW) experiment [*Gustafsson et al.*, 2001], the FluxGate Magnetometer (FGM) [*Balogh et al.*, 2001], the Spatio-Temporal

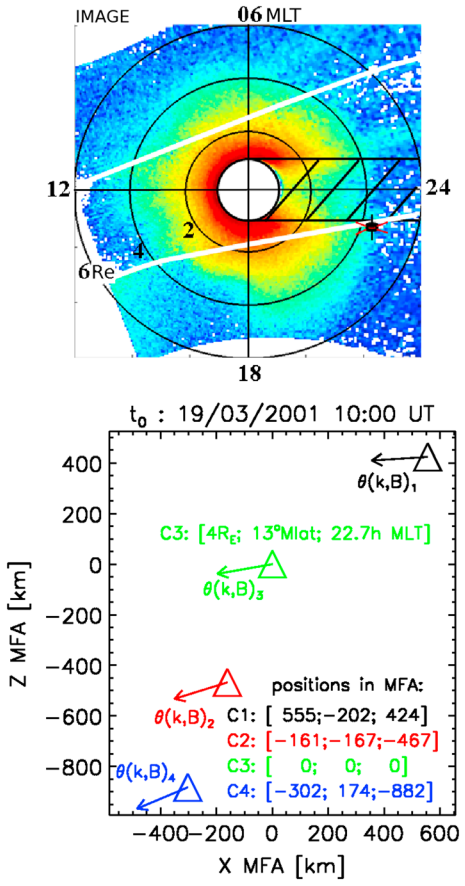

Figure 1. (top) EUV image of the plasmasphere, projected onto the magnetic equatorial plane, at 1016 UT (19 March 2001) with the projection of the Cluster spacecraft location. The inner black circle corresponds to the approximate size and position of the Earth, with its shadow extending toward the opposite direction to the Sun. White lines mark the separation between the field of views of the three IMAGE/EUV cameras. (bottom) Cluster positions at t_0 (1000 UT on 19 March 2001) projected onto ($\mathbf{X}_{MFA}$, $\mathbf{Z}_{MFA}$) plane. C3 location is the origin of the coordinate system. The colored arrows are projection of the mean wave vector orientation at each spacecraft location onto the ($\mathbf{X}_{MFA}$, $\mathbf{Z}_{MFA}$) plane.

Analysis of Field Fluctuation (STAFF) instrument [*Cornilleau-Wehrlin et al.*, 2003], and the Waves of HIgh frequency and Sounder for Probing Electron density by Relaxation (WHISPER) instrument [*Décréau et al.*, 2001].

The extreme ultraviolet (EUV) instrument on board the Imager for Magnetopause-to-Aurora Global Exploration (IMAGE) spacecraft [*Burch*, 2000] observed sunlight resonantly scattered by He^+ ions, producing an emission at 30.4 nm [*Sandel et al.*, 2000]. EUV images are obtained every 10 min through long exposure times and long line-of-sight contributions through the optically thin plasma medium. Cluster and IMAGE missions have deeply modified our understanding of the plasmasphere [*Darrouzet et al.*, 2009; *Darrouzet and De Keyser*, 2013].

Figure 1 (top) is an EUV image of the plasmasphere on 19 March 2001 at 1016 Universal Time (UT) when the Cluster satellites exit the plasmasphere around 22.7 magnetic local time (MLT). EUV image is projected onto the magnetic equatorial plane. The four Cluster spacecraft enter and exit the plasmapause in the same order based on the plasma frequency measurements (WHISPER data, not shown): C1, C3, C2, and finally C4. The plasmapause crossings are sharp and not extended in time. Their L width is quite small, less than 0.1 R_E on average. From the observations of the inbound and outbound crossings (70 min time difference), the plasmapause is in terms of L shell 0.25 R_E farther to the Earth on the inbound orbit (4.75 R_E) than on the outbound orbit (4.50 R_E). This corresponds to an L shell contraction of the boundary at a speed less than 0.5 km/s. This plasmapause contraction can also be seen on EUV consecutive images during the same time period and gives a similar result (0.2 R_E). Note that the *Kp* index varies between 1 and 2+ during the 24 h preceding this event. This small increase of the geomagnetic activity results in a slight contraction of the plasmasphere and an inward motion of the plasmapause.

The reference time (t_0) for this study is 1000 UT, 19 March 2001. At t_0 the spacecraft are already present inside the plasmasphere for almost 1 h, and they are located north of the magnetic equator, moving toward higher latitudes. Spacecraft separations vary from 300 km to 1500 km, and the background magnetic field ($\mathbf{B_0}$) orientation varies by 10° or less between spacecraft locations (not shown). We define the mean magnetic field $\mathbf{B}_{mean}$ by averaging the four spacecraft measurements ($|\mathbf{B}_{mean}|$ =456 nT). We consider a magnetic field-aligned (MFA) coordinate system centered on the reference spacecraft, C3. $\mathbf{Z}_{MFA}$ axis lies along $\mathbf{B}_{mean}$, and the ($\mathbf{X}_{MFA}$, $\mathbf{Z}_{MFA}$) plane contains $\mathbf{B}_{mean}$ and the Earth. We choose $\mathbf{X}_{MFA}$ with an anti-earthward orientation, and $\mathbf{Y}_{MFA}$ is completing the right-hand system ($\mathbf{Y}_{MFA}$ points dawnward). Figure 1(bottom) presents the spacecraft positions in the ($\mathbf{X}_{MFA}$, $\mathbf{Z}_{MFA}$) plane. Colored arrows represent the mean propagation angles (cf. next section). It is obvious that C2, C3, and C4 are almost aligned in that plane and that C1 deviates a bit from this alignment. The spacecraft are regularly spaced along $\mathbf{B}_{mean}$ by about 400 km in the following order: C4, C2, C3, and C1. The four spacecraft follow the same order along $\mathbf{X}_{MFA}$ axis, C4 being the closest from both Earth and the magnetic equatorial plane. Spacecraft separations are lower than 400 km along $\mathbf{Y}_{MFA}$.

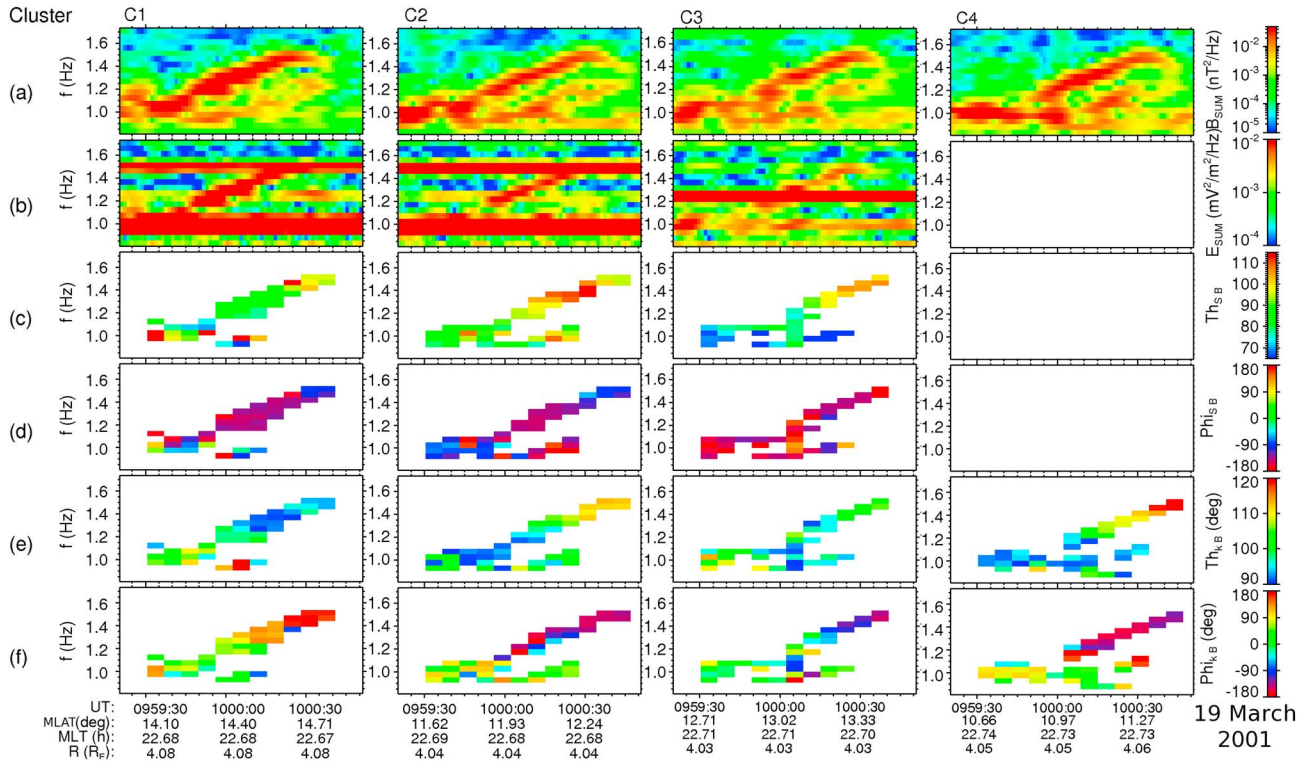

Figure 2. Analysis of the 5*5 spectral matrices derived from the three components of the wave magnetic field and two components of the wave electric field of the Cluster spacecraft (from left to right: C1 to C4). (a) Magnetic PSD, (b) electric PSD, (c) $\theta_{\mathbf{S},\mathbf{B_0}}$, (d) $\phi_{\mathbf{S},\mathbf{B_0}}$, (e) $\theta_{\mathbf{k},\mathbf{B_0}}$, and (f) $\phi_{\mathbf{k},\mathbf{B_0}}$ (from top to bottom). Electric data are not available for C4. The intense lines seen on the electric PSD (Figure 2b) are spin harmonic effects.

3. Spectral Matrices Analysis

In Figure 2, we analyze the 5*5 spectral matrices (SM) derived from the three components of the wave magnetic field **B** (STAFF instrument) and two components of the wave electric field **E** (EFW instrument) for C1, C2, C3, and C4 (from left to right). No electric data are available for C4. As noted in paper 1, a similar tone is observed on the four magnetic power spectral density (PSD) spectrograms (Figure 2a). Harmonics of the spin frequency shadow the electric PSD spectrograms (Figure 2b). Nevertheless, the electric counterpart of the rising tone is partially seen.

Santolík et al. [2001] describe how to derive the Poynting flux (**S**) orientation from the SM in the frequency domain. The deviation angle ($\theta_{\mathbf{S},\mathbf{B_0}}$) of **S** from $\mathbf{B_0}$ is obtained assuming that **E** and **B** are perpendicular. For $\theta_{\mathbf{S},\mathbf{B_0}} = 0°$ **S** is field aligned. $\theta_{\mathbf{S},\mathbf{B_0}}$ varies between 0° and 180°. With the same assumption, we obtain the azimuthal angle $\phi_{\mathbf{S},\mathbf{B_0}}$ of **S** in the plane perpendicular to $\mathbf{B_0}$. $\phi_{\mathbf{S},\mathbf{B_0}}$ varies from −180 to 180°, $\mathbf{S}_\perp$ points dawnward for positive values of $\phi_{(\mathbf{S},\mathbf{B_0})}$ and outward from the Earth for $\phi_{(\mathbf{S},\mathbf{B_0})} = 0°$. $\theta_{\mathbf{S},\mathbf{B_0}}$ and $\phi_{\mathbf{S},\mathbf{B_0}}$ are plotted on Figures 2c and 2d, respectively. Overall frequencies $\theta_{\mathbf{S},\mathbf{B_0}}$ values of the rising tone vary in a [80; 110]° interval, indicative of an energy propagation mainly transverse to $\mathbf{B_0}$ (Figure 2c). The propagation is the most oblique for C1, and it is clearly antifield aligned at C2 location. These results can explain why no clear conclusion could be drawn in paper 1 from the analysis of the $S_\parallel$ sign. $|\phi_{\mathbf{S},\mathbf{B_0}}|$ values of the rising tone vary in a [−90; −180]° interval (Figure 2d): the tone propagates deeper in the plasmapause, roughly toward the Earth.

Singular Value Decomposition analysis of the SM magnetic components [*Santolík et al.*, 2003a] shows that the propagation angle inclination $\theta_{\mathbf{k},\mathbf{B_0}}$ is oblique at C4 location (paper 1). This is also valid for the other spacecraft (Figure 2e). From SM magnetic components, **k** orientation can be determined with a 180° uncertainty. We compute the average values, normalized by the corresponding PSD, of $\theta_{\mathbf{k},\mathbf{B_0}}$ and of the propagation angle azimuth $\phi_{\mathbf{k},\mathbf{B_0}}$ (Figure 2f) over the same rising tone on each of the four spacecraft. The two possible solutions are $(\theta_{\mathbf{k},\mathbf{B_0}}; \phi_{\mathbf{k},\mathbf{B_0}}) = (75°; 31°)$ and $(\theta_{\mathbf{k},\mathbf{B_0}}; \phi_{\mathbf{k},\mathbf{B_0}}) = (105°; -149°)$. **S** and **k** are expected to have similar directions as indicated by the numerical solutions given by the WHAMP (Waves in Homogeneous Anisotropic

Multicomponent Plasmas) code [*Rönnmark*, 1982]. The (**k**, **S**) angle is lower than 5° and increases with increasing **k** and/or decreasing $\theta_{\mathbf{k},\mathbf{B_0}}$ (not shown). We thus choose the second possibility: both **k** and **S** are directed toward the Earth and toward the equatorial plane. For C1, C2, and C3, $\theta_{\mathbf{S},\mathbf{B_0}}$ is larger than $\theta_{\mathbf{k},\mathbf{B_0}}$ by ~10°. The observed difference is larger than expected but still small. It is probably caused by the complexity of the wave field and/or by small artificial phase shifts induced by using both magnetic and electric antennas in the measurement of $\theta_{\mathbf{S},\mathbf{B_0}}$.

$\theta_{\mathbf{k},\mathbf{B_0}}$ varies inside each tone and from one spacecraft to the other (Figure 2e). We use the numerical values of each record to refine our analysis. On average, $\theta_{\mathbf{k},\mathbf{B_0}}$ varies by 10° in 2° MLAT (between C1 and C4): $\theta_{\mathbf{k},\mathbf{B_0}}$ tends to be more parallel toward lower latitudes. In Figure 1, the colored arrows, inclined by the mean $\theta_{\mathbf{k},\mathbf{B_0}}$ observed at each spacecraft, illustrate this effect. At C1, the value is always high: between 93° and 95°. At C2, C3, and C4 locations, $\theta_{\mathbf{k},\mathbf{B_0}}$ turns less oblique with increasing frequency: from 99° to 115°, from 98° to 106°, and from 107° to 124°, respectively. $\theta_{\mathbf{k},\mathbf{B_0}}$ versus frequency variation is higher at lower magnetic latitudes. From Figure 2f we note that $\phi_{\mathbf{k},\mathbf{B_0}}$ orientation is clearly anti-earthward and also duskward for C2, C3, and C4 (negative values).

4. Waveform Analysis

The wave packet fine structure of rising tones has been studied from theory, observations, and simulations [*Omura et al.*, 2010; *Shoji and Omura*, 2013; *Nakamura et al.*, 2015]. The wave packet formation starts with a linear amplification stage. When the wave amplitude reaches the nonlinear threshold, a triggered emission is generated at a higher frequency, the nonlinear wave growth takes place, and the wave packet is released. The frequency increases only inside wave packets. The instantaneous frequency of the rising tones is commonly used to study the wave packets [*Santolík et al.*, 2003b, 2004; *Omura et al.*, 2010; *Kurita et al.*, 2012; *Santolík et al.*, 2014]. The presence of other emissions in the same time and in the same frequency range of the presently studied rising tones (cf. Figure 2a) makes the instantaneous frequency analysis tricky. We hereafter rather study the filtered waveform in three wave packet frequency bands. Figure 3 presents time series of the field-aligned component of the magnetic wave field measured by the four STAFF instruments during the same 110 s time interval. The wave amplitudes are much larger along that component than along the two others. This is related to the almost perpendicular orientation of the wave vector and indicative of an X-mode propagation. The frequency ranges of filtered waveforms (Figures 3a–3c) are (1.15–1.30) Hz, (1.31–1.40) Hz, and (1.40–1.47) Hz, respectively. Each color refers to a given spacecraft. In Figures 3a–3c, a single large-amplitude wave packet per spacecraft is detected. The higher the frequency is, the later the wave packet is detected: these are the rising tones. It confirms the emission frequency with time increase noted in paper 1 after Fourier analysis. The times of amplitude maxima ($t_{i,l}$, where i is the spacecraft number and l the panel letter) are marked by vertical colored dashed lines. In each panels, $t_{i,l}$ is recorded in the same order: $t_{1,l}$, then $t_{3,l}$, $t_{2,l}$, and finally $t_{4,l}$. We recall here that the spacecraft are orbiting in this order along $-\mathbf{X}_{\mathrm{MFA}}$ and $-\mathbf{Z}_{\mathrm{MFA}}$ (cf. section 2). The sense of propagation of the wave packets is consistent with the Poynting flux analysis. The wave maximum amplitude decreases with increasing frequency.

Using $t_{i,l}$, we reconstruct the frequency sweep rate of the rising tones at each spacecraft. The mean value and the standard deviation are 9.2×10^{-3}Hz/s $\pm$ 5×10^{-4} Hz/s. All four rising tones have a similar slope. The mean value matches the slope estimated in Table 3 of paper 1 from PSD observations (9.6×10^{-3} Hz/s). The low standard deviation value supports the hypothesis that all spacecraft detect the same rising tone that propagates along $-\mathbf{X}_{\mathrm{MFA}}$ and $-\mathbf{Z}_{\mathrm{MFA}}$.

In addition to $t_{i,l}$, we now also consider the spacecraft pair separations ($\Delta\mathbf{r_{ij}} = \mathbf{r_i} - \mathbf{r_j}$), where $\mathbf{r_i}$ stands for spacecraft i position. Assuming that the emission propagates between two spacecraft at a constant group velocity ($\mathbf{v_{Gl}}$) for a frequency range l defined previously, we have the following relationship between $\Delta t_{ij,l} = t_{i,l} - t_{j,l}$, $\Delta\mathbf{r_{i,j}}$, and $\mathbf{v_{Gl}}$ (see *Santolík et al.* [2005], neglecting the orbital velocity and in the plasma frame):

$$\Delta t_{ij,l} = \Delta\mathbf{r_{ij}}.\mathbf{v_{Gl}}/v_{Gl}^2 \tag{1}$$

We have 6 spacecraft pairs to estimate $\mathbf{v_G}$ for each of the three wave packets using a nonlinear regression and a timing accuracy of one wave period. Obtained group velocities are 192, 166, and 193 km/s for wave packet #1, #2, and #3, respectively. The standard deviations are larger than 40 km/s. These high values are indicative of quick changes in the group velocity, which is frequency and location dependent. We compute also the velocities pair by pair, assuming constant propagation and testing various propagation angles. We emphasize here that no result gives indication of a group velocity much larger than 200 km/s.

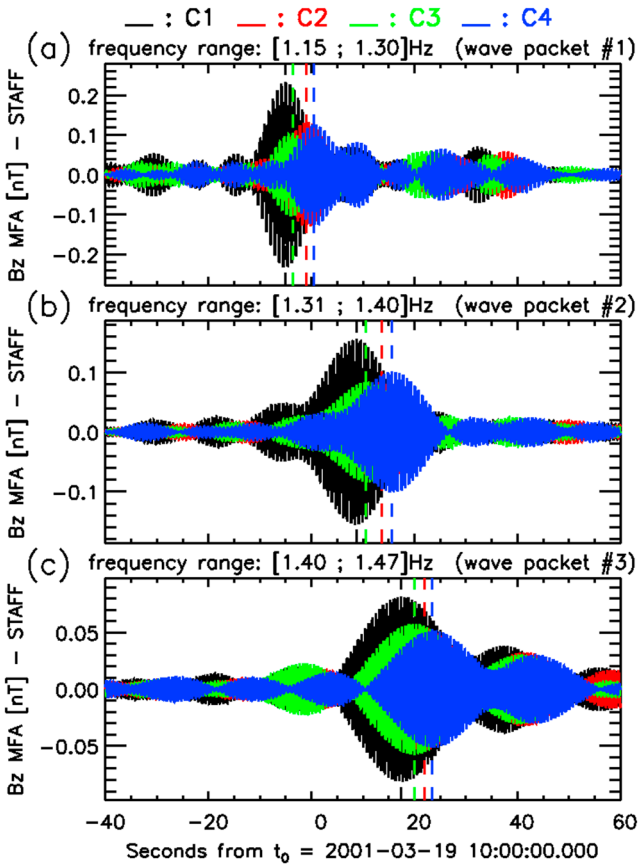

Figure 3. Field-aligned component of filtered magnetic waveforms observed by Cluster spacecraft around t_0 for (a–c) three frequency ranges. Vertical dashed lines mark the waveform maximum recorded at each spacecraft during the displayed time and frequency ranges.

5. Comparisons With Theoretical Results

We compare observational results with the numerical solutions given by the WHAMP code. We consider four cold (~10 eV) Maxwellian populations: H^+, He^+, O^+, and e^-. Precise density measurements are missing: The spacecraft potentials are saturated, the plasma frequency is above the frequency range of the WHISPER instrument, and the particle instruments do not catch the full cold plasma population. We choose two compositions that match with observational results: $(n_{H^+}; n_{He^+}; n_{O^+})_1 = (460; 70; 70)\ cm^{-3}$ and $(n_{H^+}; n_{He^+}; n_{O^+})_2 = (1140; 110; 50)\ cm^{-3}$. The relative abundances in $(n_{H^+}; n_{He^+}; n_{O^+})_1$ are close to the one estimated in *Pickett et al.* [2010]. The total density of 600 cm^{-3} in $(n_{H^+}; n_{He^+}; n_{O^+})_1$ and the ~10% relative abundance of He^+ in $(n_{H^+}; n_{He^+}; n_{O^+})_2$ are typical for the outer plasmasphere [*Farrugia et al.*, 1989; *Sandel*, 2011]. Figure 4 presents the evolution of frequency versus $k_\perp$ (Figure 4a), group velocity versus frequency (Figure 4b), and moduli of the perpendicular electric field components versus frequency (Figure 4c). Plain (respectively dotted) lines are WHAMP results for plasma composition $(n_{H^+}; n_{He^+}; n_{O^+})_1$ (respectively, $(n_{H^+}; n_{He^+}; n_{O^+})_2$). The runs are performed with the mean $|\mathbf{B_0}|$ (456 nT) and the mean propagation angle (75°). Values of experimental results are displayed by colored squares and lines: red, green, and blue for wave packet #1, #2 and #3, respectively. In Figure 4a, dashed lines mark the wave packet frequency domains and the corresponding wave vector domains. In Figure 4b, the horizontal dashed bars, given by the frequency extent in Figure 4a, and the vertical dashed bars, given by the computed velocity standard deviation, can be interpreted as error bars.

Other important properties of the mode are the following (not shown): the polarization is right hand, $\theta_{\mathbf{S},\mathbf{B_0}}$ and $\theta_{\mathbf{k},\mathbf{B_0}}$ have the same direction, the mode is already strongly damped at $f = 0.22 f_{H^+}$, and the mode resonates above f_{He^+} ($= 0.25 f_{H^+}$). These properties match with the EMIC mode 4 described in *Horne and Thorne* [1993]. For both plasma compositions the observed group velocities match with the theoretical ones (Figure 4b). It is necessary for both plasma compositions to have a large relative abundance of O^+ as compared to the

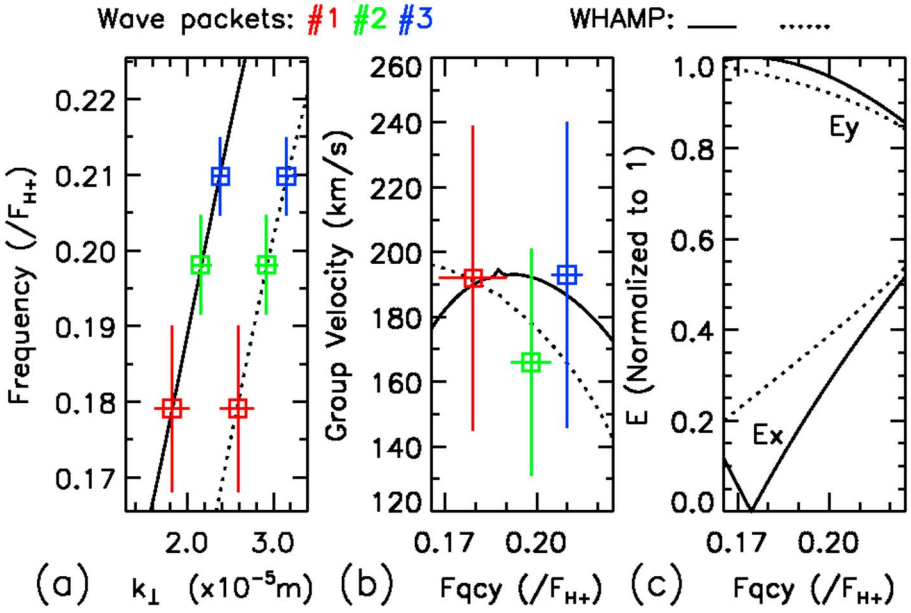

Figure 4. Comparison of observations (colored squares and lines) to numerical computation results for two different plasma compositions: $(n_{H^+}; n_{He^+}; n_{O^+})_1 = (460; 70; 70)\ cm^{-3}$ (plain black lines) and $(n_{H^+}; n_{He^+}; n_{O^+})_2 = (1140; 110; 50)\ cm^{-3}$ (dotted black lines). Frequency versus $k_\perp$, group velocity versus frequency, and perpendicular electric field components versus frequency.

typical one (~1% [*Farrugia et al.*, 1989]). This was also the case in a previous study of EMIC TEs, based on cutoff frequency observations [*Pickett et al.*, 2010].

A normalized *Ey* value close to 1 indicates that the major axis of wave electric field polarization ellipse is perpendicular to **k** (Figure 4c). We note that in the SR2 (Spin Reference 2) coordinate system almost all the measured electric field spectral densities lie along the Y_{SR2} direction (not shown). As the X_{SR2} component contains roughly the spacecraft-Earth direction, it means that **k** lies mainly along the X_{SR2} axis direction, which is mainly earthward. It confirms our results on the Poynting vector and wave vector directions from section 3.

6. Discussion

The EMIC propagation in the magnetosphere has been studied with ray tracing analysis [*Rauch and Roux*, 1982; *Horne and Thorne*, 1993]. The *Horne and Thorne* [1993] study is the most relevant in the present case as they tested the propagation of every EMIC mode propagating in a H^+, He^+, and O^+ plasma. The propagation of the observed mode is described in details in their Figure 12 and related comments. The ray is launched at the plasmapause in the equatorial plane with a frequency between f_{He^+} and f_{H^+}, above the crossover frequency. It returns back close to its launch place after a loop, being reflected twice and crossing the magnetic equator deep in the plasmasphere. After a loop, the wave gain is about 2×10^{-2}.

We estimate that we observe part of motion after a reflection, when the wave propagates toward the magnetic equatorial plane in the plasmapause. The scenario matches pretty well with our observations: the wave frequency is expected to be lower than the local f_{He^+}, after being reflected, due to the encounter of a stronger magnetic field as EMIC waves propagate deeper in the plasmasphere. The wave power is low compared to the other events reported in paper 1. We might therefore observe the wave in its second loop.

As a conclusion, we observe a reflected EMIC-triggered emission probably generated with a left-hand polarization in the equatorial region of the nightside plasmapause between the local f_{He^+} and f_{H^+}, above the crossover frequency. The triggered emission is thus observed below f_{He^+} but was generated above it, at further distance from the Earth. Observations also suggest that there is an azimuthal motion toward the afternoon side. TEs with the largest possible frequency extent are the TEs generated in the proton branch above the crossover frequency. As shown here these waves are reflected before reaching the ionosphere. It explains why TEs with large-frequency extent have not been reported from ground observations.

Following *Horne and Thorne* [1993] we consider that reflection occurs when the parallel group velocity sign reverses. The wave reflection takes place close to the bi-ion hybrid frequency when the propagation angle is about 90°. As the wave moves away from the equator, the normalized frequencies of the tone turn lower as $\mathbf{B_0}$ intensifies. The lowest-frequency part of the rising tone is reflected first, when reaching the local bi-ion hybrid frequency. The highest-frequency part of the tone will travel farther from the equator before getting reflected. This is in good accordance with our observations. The lowest-frequency part of the rising tone of C1 has the most inclined propagation angle (~95°). It is also the spacecraft at the highest-magnetic latitude. Following this scenario the tone slope will be shallower when the waves travel back toward the equatorial plane, where our observations take place. In paper 1 the slope for this event was twice shallower than for the other events, all detected moving away from the equator region. Group velocity deceleration with increasing frequency is suggested to explain this latitudinal effect. A precise ray tracing analysis can quantify the influence of each of these two effects. EMIC TEs are formed of several wave packets of increasing frequency [*Omura et al.*, 2010; *Shoji and Omura*, 2013]. In the present case we could identify three of them. After a longer journey than the one observed here (more reflections or a propagation toward the Earth), the wave packets could get separated in time due to their various frequencies. Over time, they could thus look very similar to the so-called pearl pulsations on a time-frequency spectrogram [see *Kangas et al.*, 1998, and references therein]. It is worth to notice that the reflection conserves the rising tone appearance of the emissions.

7. Conclusion

On 19 March 2001, the Cluster fleet recorded an electromagnetic rising tone on the nightside of the plasmasphere around 1000 UT. Based on its shape and the sequence of spacecraft observations, we establish that it is the same rising tone. As reported in paper 1, this right-hand polarized emission is observed below local f_{He^+} with a very oblique propagation angle. From multispacecraft analysis, we show that the emission propagates earthward, deeper in the plasmasphere and at the same time toward the equatorial region and toward the afternoon side of the plasmasphere. The group velocity is at most 200 km/s. It implies a large abundance of heavy ions (O^+).

The group velocity, polarization, frequency extent, and propagation angle of the emissions match well with the theoretical WHAMP results. The dispersion relation corresponds to EMIC mode 4 as studied in *Horne and Thorne* [1993] with their ray tracing analysis. Our observations agree with the scenario of a wave reflection above the C1 location. We conclude that the observed rising tone is an EMIC-triggered emission generated at the nightside plasmapause above the local crossover frequency of the proton branch. The tone should be progressively damped after several reflections. Our results confirm that TEs with large-frequency extent cannot be detected from the ground. Having four points of measurement in space gives an access to both spatial and temporal evolution of the propagation angle, which varies quickly both in frequency and in magnetic latitude. The magnetic latitude of the reflection point increases with frequency: Reflected tone has a shallower slope than the incoming one. The reflection explains thus the shallow slope noted in paper 1.

This unique case study can be used as a reference for a future ray tracing analysis in order to locate the generation site, the place of reflection, and to test pearl pulsation formations.

Acknowledgments
We acknowledge the ESA Cluster Science Archive (http://cosmos.esa.int/csa), the EFW and FGM teams for making the Cluster data publicly available. We acknowledge support of GACR P209/12/2394 grant, the Praemium Academiae Award, and the LH15304 program. F. Darrouzet acknowledges Belspo (Belgian Federal Science Policy Office) through a Prodex project (contract PEA-C4000109739). We acknowledge G. Belmont, P. Robert (LPP/CNRS), and L. Rezeau (LPP/Univ. Paris 6) for the WHAMP code version used in this study. IMAGE/EUV data are available at http://euv.lpl.arizona.edu/euv. We acknowledge Dennis Gallagher (NASA) for the EUV image projection code.

References

Balogh, A., et al. (2001), The Cluster magnetic field investigation: Overview of in-flight performance and initial results, *Ann. Geophys.*, *19*(10/12), 1207–1217, doi:10.5194/angeo-19-1207-2001.

Burch, J. (2000), IMAGE mission overview, *Space Sci. Rev.*, *91*(1), 1–14, doi:10.1023/A:1005245323115.

Cornilleau-Wehrlin, N., et al. (2003), First results obtained by the Cluster STAFF experiment, *Ann. Geophys.*, *21*(2), 437–456, doi:10.5194/angeo-21-437-2003.

Darrouzet, F., and J. De Keyser (2013), The dynamics of the plasmasphere: Recent results, *J. Atmos. Sol. Terr. Phys.*, *99*, 53–60, doi:10.1016/j.jastp.2012.07.004.

Darrouzet, F., J. De Keyser, and V. Pierrard (Eds.) (2009), *The Earth's Plasmasphere: A Cluster and Image Perspective*, 296 pp., Springer, New York.

Décréau, P. M. E., et al. (2001), Early results from the WHISPER instrument on Cluster: An overview, *Ann. Geophys.*, *19*(10/12), 1241–1258, doi:10.5194/angeo-19-1241-2001.

Escoubet, C., R. Schmidt, and M. Goldstein (1997), Cluster—Science and mission overview, *Space Sci. Rev.*, *79*(1–2), 11–32, doi:10.1023/A:1004923124586.

Farrugia, C. J., D. T. Young, J. Geiss, and H. Balsiger (1989), The composition, temperature, and density structure of cold ions in the quiet terrestrial plasmasphere: GEOS 1 results, *J. Geophys. Res.*, *94*(A9), 11,865–11,891, doi:10.1029/JA094iA09p11865.

Grison, B., O. Santolík, N. Cornilleau-Wehrlin, A. Masson, M. J. Engebretson, J. S. Pickett, Y. Omura, P. Robert, and R. Nomura (2013), EMIC triggered chorus emissions in Cluster data, *J. Geophys. Res. Space Physics*, *118*, 1159–1169, doi:10.1002/jgra.50178.

Gustafsson, G., et al. (2001), First results of electric field and density observations by Cluster EFW based on initial months of operation, *Ann. Geophys.*, *19*(10/12), 1219–1240, doi:10.5194/angeo-19-1219-2001.

He, Z., Q. Zong, S. Liu, Y. Wang, R. Lin, and L. Shi (2014), Frequency sweep rates of rising tone electromagnetic ion cyclotron waves: Comparison between nonlinear theory and Cluster observation, *Phys. Plasmas*, *21*(12), 122309, doi:10.1063/1.4905065.

Horne, R. B., and R. M. Thorne (1993), On the preferred source location for the convective amplification of ion cyclotron waves, *J. Geophys. Res.*, *98*(A6), 9233–9247, doi:10.1029/92JA02972.

Kangas, J., A. Guglielmi, and O. Pokhotelov (1998), Morphology and physics of short-period magnetic pulsations, *Space Sci. Rev.*, *83*, 435–512, doi:10.1023/A:1005063911643.

Kurita, S., Y. Katoh, Y. Omura, V. Angelopoulos, C. M. Cully, O. Le Contel, and H. Misawa (2012), Themis observation of chorus elements without a gap at half the gyrofrequency, *J. Geophys. Res.*, *117*, A11223, doi:10.1029/2012JA018076.

Nakamura, S., Y. Omura, S. Machida, M. Shoji, M. Nosé, and V. Angelopoulos (2014), Electromagnetic ion cyclotron rising tone emissions observed by THEMIS probes outside the plasmapause, *J. Geophys. Res. Space Physics*, *119*, 1874–1886, doi:10.1002/2013JA019146.

Nakamura, S., Y. Omura, M. Shoji, M. Nosé, D. Summers, and V. Angelopoulos (2015), Subpacket structures in EMIC rising tone emissions observed by the THEMIS probes, *J. Geophys. Res. Space Physics*, *120*, 7318–7330, doi:10.1002/2014JA020764.

Omura, Y., J. Pickett, B. Grison, O. Santolik, I. Dandouras, M. Engebretson, P. M. E. Décréau, and A. Masson (2010), Theory and observation of electromagnetic ion cyclotron triggered emissions in the magnetosphere, *J. Geophys. Res.*, *115*, A07234, doi:10.1029/2010JA015300.

Pickett, J. S., et al. (2010), Cluster observations of EMIC triggered emissions in association with Pc1 waves near Earth's plasmapause, *Geophys. Res. Lett.*, *37*, L09104, doi:10.1029/2010GL042648.

Rauch, J. L., and A. Roux (1982), Ray tracing of ULF waves in a multicomponent magnetospheric plasma: Consequences for the generation mechanism of ion cyclotron waves, *J. Geophys. Res.*, *87*(A10), 8191–8198, doi:10.1029/JA087iA10p08191.

Rönnmark, K. (1982), Waves in Homogeneous, Anisotropic Multicomponent Plasmas (WHAMP), *IRF Sci. Rep. 179*, Kiruna Geophysical Institute, Kiruna, Sweden.

Sandel, B. R. (2011), Composition of the plasmasphere and implications for refilling, *Geophys. Res. Lett.*, *38*(14), L14104, doi:10.1029/2011GL048022.

Sandel, B. R., et al. (2000), The extreme ultraviolet imager investigation for the IMAGE mission, *Space Sci. Rev.*, *91*, 197–242.

Santolík, O., F. Lefeuvre, M. Parrot, and J. L. Rauch (2001), Complete wave-vector directions of electromagnetic emissions: Application to INTERBALL-2 measurements in the nightside auroral zone, *J. Geophys. Res.*, *106*, 13,191–13,202, doi:10.1029/2000JA000275.

Santolík, O., M. Parrot, and F. Lefeuvre (2003a), Singular value decomposition methods for wave propagation analysis, *Radio Sci.*, *38*(1), 1010, doi:10.1029/2000RS002523.

Santolík, O., D. A. Gurnett, J. S. Pickett, M. Parrot, and N. Cornilleau-Wehrlin (2003b), Spatio-temporal structure of storm-time chorus, *J. Geophys. Res.*, *108*(A7), 1278, doi:10.1029/2002JA009791.

Santolík, O., D. A. Gurnett, J. S. Pickett, M. Parrot, and N. Cornilleau-Wehrlin (2004), A microscopic and nanoscopic view of storm-time chorus on 31 March 2001, *Geophys. Res. Lett.*, *31*, L02801, doi:10.1029/2003GL018757.

Santolík, O., A. M. Persoon, D. A. Gurnett, P. M. E. Décréau, J. S. Pickett, O. Maršálek, M. Maksimovic, and N. Cornilleau-Wehrlin (2005), Drifting field-aligned density structures in the night-side polar cap, *Geophys. Res. Lett.*, *32*, L06106, doi:10.1029/2004GL021696.

Santolík, O., C. A. Kletzing, W. S. Kurth, G. B. Hospodarsky, and S. R. Bounds (2014), Fine structure of large-amplitude chorus wave packets, *Geophys. Res. Lett.*, *41*, 293–299, doi:10.1002/2013GL058889.

Shoji, M., and Y. Omura (2011), Simulation of electromagnetic ion cyclotron triggered emissions in the Earth's inner magnetosphere, *J. Geophys. Res.*, *116*, A05212, doi:10.1029/2010JA016351.

Shoji, M., and Y. Omura (2013), Triggering process of electromagnetic ion cyclotron rising tone emissions in the inner magnetosphere, *J. Geophys. Res. Space Physics*, *118*, 5553–5561, doi:10.1002/jgra.50523.

Shoji, M., Y. Omura, B. Grison, J. Pickett, I. Dandouras, and M. Engebretson (2011), Electromagnetic ion cyclotron waves in the helium branch induced by multiple electromagnetic ion cyclotron triggered emissions, *Geophys. Res. Lett.*, *38*, L17102, doi:10.1029/2011GL048427.

Young, D. T., S. Perraut, A. Roux, C. de Villedary, R. Gendrin, A. Korth, G. Kremser, and D. Jones (1981), Wave-particle interactions near Ω_{He+} observed on GEOS 1 and 2. I—Propagation of ion cyclotron waves in He^+-rich plasma, *J. Geophys. Res.*, *86*, 6755–6772, doi:10.1029/JA086iA08p06755.